

**Large antiferromagnetic fluctuation enhancement of the thermopower
at a critical doping in magnetic semimetal $\text{Cr}_{1+\delta}\text{Te}_2$**

*Atwa Mohamed¹, Yuita Fujisawa¹, Takatsugu Onishi¹, Markel Pardo-Almanza¹, Mathieu Couillard¹,
Keita Harada¹, Tsunehiro Takeuchi², Yoshinori Okada¹*

¹Quantum Materials Science Unit, Okinawa Institute of Science and Technology (OIST),

Okinawa 904-0495, Japan

²Research Center for Smart Energy Technology, Toyota Technological Institute,

Nagoya 468-8511, Japan;

Abstract

$\text{Cr}_{1+\delta}\text{Te}_2$ is a self-intercalated transition metal dichalcogenide that hosts tunable electronic filling and magnetism in its semimetallic band structure. Recent angle-resolved photoemission spectroscopy (ARPES) studies have unveiled a systematic shift in this semimetallic band structure relative to the chemical potential with increased Cr doping. This report presents the temperature and magnetic field dependence of the longitudinal thermopower S_{xx} for different $\text{Cr}_{1+\delta}\text{Te}_2$ compositions. We show that as doping increases, the sign of S_{xx} changes from positive to negative at the critical doping level of $\delta \sim 0.5$. This observed doping-dependent trend in the thermopower is consistent with the evolution of the semimetallic band structure from ARPES. Importantly, an anomalous enhancement of the thermoelectric response near T_C is also observed around $\delta \sim 0.5$. Combining information from magnetometry and ARPES measurements, existence of the critical nature of the doping level $\delta_c (\sim 0.5)$ is unveiled in magnetic semimetal $\text{Cr}_{1+\delta}\text{Te}_2$, where antiferromagnetic fluctuation and near-Fermi-energy pseudogap formation play a potential vital role in enhancing thermoelectric energy conversion.

Introduction

The thermoelectric effect enables the conversion of thermal energy to electricity¹. Asymmetry in the energy-dependent electronic conductivity between the hot and cold sides of a metallic conductor generates a driving force for a net flow of charge entropy. Whatever the microscopic origins of this entropy are, if they are coupled to charge carriers through inelastic scattering, one can imagine various intriguing ways to modulate thermoelectric effects. Manipulation of the magnetic degree of freedom is another attractive route to controlling the thermoelectric effect. For example, while a consensus has yet to be reached, a large spin entropy and anomalous electronic states near E_F have been proposed to explain the giant Seebeck effect of cobalt oxides^{2,3,4,5}. Efforts to simultaneously engineer the heat, spin, and charge degrees of freedom have resulted in the field of spin caloritronics, where spin currents control and enhance thermoelectric phenomena^{6,7,8,9,10}. Magnetic fluctuation driven enhancement of the thermopower has been reported, for example, in a Heusler compound¹². Antiferromagnetism enhanced thermoelectricity has garnered considerable interest in from both a fundamental and practical perspective^{13,14}. Research on the interaction between improved thermoelectric response and Berry curvature physics is also ongoing^{15,16,17}. Although these recent explorations of the exotic interplay between magnetism and the thermoelectric response are promising, a microscopic understanding of the coupling between magnetism and thermoelectricity is still in its infancy. To promote understanding of the interaction between spins and charges in thermoelectric materials, ideal materials to focus on are those with widely tunable electronic band filling and deeply controllable magnetic structure.

Transition-metal dichalcogenides (TMDs) are a unique platform for tuning electronic and magnetic properties in low dimension. The atomic layers of TMDs are weakly coupled through the van der Waals (vdW) force, creating an opportunity to chemically tune their physical properties by intercalating native atoms into the vdW gaps¹⁸. Among the magnetic TMDs, $\text{Cr}_{1+\delta}\text{Te}_2$ (**Fig. 1a**) is a promising self-intercalated ferromagnet with widely-tunable electronic and magnetic properties^{19,20,21,22,23,24,25,26,27,28,29,30,31,32,33,34,35,36,37}. Our recent efforts have yielded a unique recipe for the growth of epitaxial thin films of $\text{Cr}_{1+\delta}\text{Te}_2$ over a wide compositional range³⁸. Based on the previously reported phase diagram of this system, a Curie temperature (T_c) beyond room temperature is achieved as the intercalated Cr (δ) increases (**Fig. 1b left axis**). Furthermore, the effective magnetic anisotropy energy (K_{eff}), defined as the difference in energy to align spins along the in-plane (K_{in}) or out-of-plane (K_{out}) directions, shows a gradual change from positive to negative values as δ increases (**Fig. 1b right axis**). Density functional theory (DFT) calculations have suggested an inherent magnetic frustration from competing magnetic interactions, which plays a role in modulating K_{eff} in this system. This K_{eff} modulation yielding enhanced magnetic fluctuation at $K_{eff}\sim 0$ has been speculated in literature³⁸.

Recently, the doping-dependent electronic structure of $\text{Cr}_{1+\delta}\text{Te}_2$ has also been reported. Using in-situ angle-resolved photoemission spectroscopy (ARPES), a systematic energy shift of the semimetallic band portion was directly revealed around the zone boundary relative to the chemical potential (**Figs. 1c and d**)³⁹. ARPES measurements at 14 K (well below T_c) have yielded a characteristic energy (E_0) for the semimetallic band portion around the \bar{M} point (**Fig. 1d**). The Fermi energy E_F was shown to approach E_0 near a critical doping $\delta_c \sim 0.5$. Alongside a metallic hole band near the $\bar{\Gamma}$ point at all doping levels, the formation of a pseudogap in the

density of states (DOS) was predicted to occur around this critical composition. These ARPES findings prompted our current investigation of the doping-dependent longitudinal thermopower (S_{xx}), as its sign and absolute value should be sensitive probes of the existence of the pseudogap and its energy relative to the chemical potential. Another worthwhile motivation for measuring S_{xx} is to pursue any magnetism-driven enhancements to the thermopower that $\text{Cr}_{1+\delta}\text{Te}_2$ can be expected to host, being both magnetically and electronically tunable. However, the doping evolution of the thermoelectric response in the absence and presence of magnetic fields has not been investigated in $\text{Cr}_{1+\delta}\text{Te}_2$.

We report on the systematic measurement of S_{xx} and longitudinal electrical resistivity (ρ_{xx}) in magnetic semimetal $\text{Cr}_{1+\delta}\text{Te}_2$. We discuss the doping, temperature, and magnetic field evolution of S_{xx} with respect to the underlying band structure and magnetism. As the most significant finding in this study, we show that at the critical doping level of $\delta_c \sim 0.5$, a possible interaction between magnetic fluctuations and the formation of an anomalous electronic state at the chemical potential cooperatively leads to an enhancement of the thermoelectric properties in $\text{Cr}_{1+\delta}\text{Te}_2$.

Methods

Sample Preparation

The (001) oriented epitaxial $\text{Cr}_{1+\delta}\text{Te}_2$ films used in this work were grown on Al_2O_3 (0001) substrates with a molecular beam epitaxy (MBE) system through a two-step process that involved film deposition followed by post-deposition annealing in situ as described in our previous work. Following the same detailed characterization methods performed previously, the fraction of intercalated Cr(δ) was determined by combining energy-dispersive X-ray spectroscopy (EDS) of the elemental ratios and X-ray diffraction (XRD) estimates of the lattice constants. The thickness of all samples grown in this study was approximately 80 nm.

Transport Measurements

S_{xx} and ρ_{xx} were measured simultaneously using a Quantum Design PPMS® DynaCool system combined with a custom-built sample stage and electronics set-up. The electrode configuration is shown in **Fig. 2a**. In this study, technical limitations in our measurement setup restrict our S_{xx} measurements between 80 and 380 K. The lower temperature limit mainly represents a threshold below which the Al_2O_3 substrate becomes too thermally conductive to maintain a sufficient temperature gradient and determine S_{xx} across the sample accurately. The vertical dotted lines in **Fig. 1b** indicate the doping levels studied in this report on the previously reported phase diagram. In this report, all magnetic fields were applied along the out-of-plane direction, as shown schematically in **Fig. 2a**.

Results and Discussion

Doping and temperature dependence of ρ_{xx} and S_{xx} in $B=0$

The temperature and doping dependence of ρ_{xx} and S_{xx} are shown in **Figs. 2b** and **c**, respectively. Regardless of the detailed microscopic origins, suppression of electron-spin scattering can be expected to occur in magnetically-ordered states compared to paramagnetic states. Therefore, T_C at each doping level is estimated

from the position of the kink in the $\rho_{xx}(T)$ curves, as indicated by the arrows in **Figs. 2b** and **c**. The estimated T_C values are consistent with those determined previously³⁸. The doping dependence of $S_{xx}(T)$ also exhibits several characteristic behaviors. The samples with $\delta=0.34$ and $\delta=0.4$ show positive values with a nearly linear T dependence (left two panels in **Fig. 2c**). In contrast, S_{xx} for $\delta=0.50$ and $\delta=0.54$ (middle panel in **Fig. 2c**) show negative values with a kink around T_C . Notably, such a kink structure around T_C is nearly absent in the highest doped sample, $\delta=0.68$ (right panel in **Fig. 2c**). Hereafter, we focus on S_{xx} , as the essential trends in $\rho_{xx}(T)$ are qualitatively similar for all doping levels. In the following sections, we elaborate on the doping-dependent sign change in $S_{xx}(T)$, followed by a discussion of the electronic and magnetic origins of the kink around T_C in the $S_{xx}(T)$ curves.

Mott formula for S_{xx}

The simplest model for the temperature dependence of thermopower S_{xx} in metals is the so-called Mott relation.

$$S_{xx} = \frac{\pi^2 k_B^2 T}{3e} \times \left\{ \frac{d \ln \sigma_{xx}(E)}{dE} \right\}_{E=E_F} = \frac{\pi^2 k_B^2 T}{3e} \left[\frac{1}{N(E_F)} \left\{ -\frac{dN(E)}{dE} \right\}_{E=E_F} + \frac{1}{\tau(E_F)} \left\{ \frac{d\tau(E)}{dE} \right\}_{E=E_F} \right] \quad (1)$$

Here, the spectral conductivity σ_{xx} is proportional to the density of states $N(E)$ and the scattering rate $\tau(E)$, based on the relaxation time approximation from Boltzmann transport theory. By assuming an energy-independent scattering rate τ in Equation (1), S_{xx} can be expressed as:

$$S_{xx} \approx \frac{\pi^2 k_B^2 T}{3e} \left[\frac{1}{N(E_F)} \left\{ -\frac{dN(E)}{dE} \right\}_{E=E_F} \right] \quad (2)$$

The above relation makes it evident that the sign of S_{xx} corresponds to that of $-dN(E)/dE_{E=E_F}$. In this case, if the chemical potential exists in a hole-like band ($-dN/dE > 0$ at E_F), the sign and slope of $S_{xx}(T)$ become correspondingly positive, while if the chemical potential exists in an electron-like band ($-dN/dE < 0$ at E_F), the sign and slope of $S_{xx}(T)$ become negative.

Relation between $S_{xx}(\delta)$ and band structure

To uncover the connection between the sign of S_{xx} and the corresponding band structure at each $\text{Cr}(\delta)$, we plot the doping dependence of S_{xx} at 350 K and its correlation with the doping evolution of the semimetallic band portion at the \bar{M} point (**Fig. 2d**). For a fair comparison, 350 K is chosen to be above T_C for all doping levels. A sign change in S_{xx} at 350 K is evident as δ increases. Considering the semimetallic band around the \bar{M} point (**Fig. 1d**), $E_F(\delta) - E_0 > 0$ leads to $-dN/dE > 0$ and consequently to a positive sign in S_{xx} . On the other hand, $E_F(\delta) - E_0 < 0$ leads to $-dN/dE < 0$, corresponding to a negative sign in S_{xx} . Admittedly, this is a simplified picture that ignores the existence of bands other than the semimetallic band around the \bar{M} point. Moreover, this simplified picture deliberately excludes the nuance of a k_z dispersion relying solely on the band dispersion around the \bar{M} point probed using the single-photon energy available in our ARPES³⁸. Nevertheless, a correlation can clearly be seen between the sign of $E_F(\delta) - E_0$ and $S_{xx}(\delta)$. This correlation implies that the previously observed ARPES band around the \bar{M} point in **Fig. 1c** governs the doping-dependent behavior of the thermoelectric properties in

this system. This simple picture is particularly justified at higher temperatures such as those examined in this study, as the near- E_F fine band structure beyond considerations of a simple picture in **Fig. 1c** is thermally smeared out even if it exists. Also, note that the doping dependence of normal Hall coefficient does not show sign change with doping δ in a previous report³⁸. However, this is not contradictory. While the normal Hall effect is more sensitive to electronic state anisotropy in momentum space at E_F ⁴⁰, S_{xx} is sensitive to electronic state anisotropy along energy axis relative to E_F .

Magnetic fluctuation driven enhancement of S_{xx}

Next, we discuss the origin of the kink in the $S_{xx}(T)$ curves across T_C . Based on Equation (1), S_{xx} can be modulated by changes to both $N(E)$ and $\tau(E)$ by the magnetic phase transition. Before discussing these quantities, we first elaborate on the nature of magnetic fluctuations above T_C . Focusing on the magnetic field dependence of S_{xx} is a rational method of investigating the influence that magnetic fluctuations have on the thermoelectric response⁴¹. **Fig. 3a** shows S_{xx} in an external magnetic field $B = 0$ (filled symbols) and 9 T (empty symbols). To quantify the magnetic field-dependent contribution, $|\Delta S_B(T)| = |S_{xx}(T)_{B=9\text{ T}} - S_{xx}(T)_{B=0\text{ T}}|$ is defined (see hatched area in **Fig. 3a**). Here, $B = 9\text{ T}$ is chosen to be large enough compared to saturation field to completely suppress magnetic fluctuations in a wide temperature region both above and below T_C ³⁸. As the application of a magnetic field 9 T suppresses magnetic fluctuations, the quantity $|\Delta S_B(T)|$ can be considered a measure of the magnetic fluctuation-related contributions to S_{xx} in the absence of a magnetic field (**Fig. 2**). Such method was previously employed in studying the magnetic fluctuation enhancement of the thermopower in Heusler alloys¹². In our case, while $|\Delta S_B(T)|$ for two doping levels $\delta = 0.34$ and 0.40 are negligible, $|\Delta S_B(T)|$ becomes prominent for other three doping levels $\delta = 0.5, 0.54,$ and 0.68 . This observation indicates that S_{xx} responds more sensitively to an external magnetic field around $\delta = 0.5$, which results in a maximum $|\Delta S_B(T)|$ at T_C around this doping level, as opposed to a monotonic increase of $|\Delta S_B(T_C)|$ with δ . Hereafter, we discuss the intertwined microscopic nature of the magnetic fluctuations and the enhancement in S_{xx} , focusing on the critical doping level $\delta \sim 0.5$, which we designate δ_c .

Spin Fluctuation vs. Magnon Pictures around T_C

We begin by discussing the microscopic picture of the fluctuating magnetism around T_C . The conventional mean-field picture for explaining magnetism in metals is known as the Stoner model. In this model, spin-degenerate bands are split into majority and minority spin bands separated by an exchange energy that is associated with the energetic cost of transitioning from paramagnetic states ($T > T_C$) to magnetically ordered states ($T < T_C$)⁴². An abrupt change in the band structure occurs near T_C per this interpretation. However, this conventional Stoner model can be excluded as the origin of the magnetic behavior in our system, as we observe signature of magnetic fluctuation far above T_C (**Fig. 3b-c**). As an alternative, we invoke the two pictures of the microscopic origins of magnetic fluctuations. The first picture is spin fluctuation theory, which has succeeded in explaining the physical properties of itinerant magnetism in various materials⁴³. The second picture relies on the collective propagations of magnetic spin precessions, known as magnons, which emerge in localized magnetically ordered states. Spin fluctuations in itinerant electron systems predominantly influence the

thermodynamic properties of weakly or nearly ferromagnetic metals, and such spin fluctuations can survive well above T_C . Although the conventional formalism of magnons supports their dominant existence only below the Curie and Néel temperatures (T_C and T_N) of localized, magnetically-ordered systems⁴⁴, magnon excitations have been shown to persist above T_C in the so-called paramagnon regime⁴⁵.

Logarithmic temperature dependence T^n

To discern the nature of the magnetic fluctuations enhancing the thermopower, examining the exponents of the logarithmic thermopower temperature dependence has been recognized as a fruitful approach¹². The exponent of $|\Delta S_B(T)|$ up to T_C was used to clarify the origin of the magnetic fluctuation enhanced thermopower. This approach is underpinned by microscopic models of the magnetic fluctuation contributions to the specific heat (C_{mag}), which are reflected in the thermopower temperature dependence below the transition temperature¹². While an itinerant spin fluctuation picture does not support the existence of a well-defined logarithmic temperature dependence⁴⁶, the magnon picture does support a logarithmic temperature dependence⁴⁷. Based on the hydrodynamic theory of magnon-electron drag⁴⁴ $|\Delta S_{xx}|$ can be expressed as:

$$|\Delta S_{xx}| = \frac{2}{3} \frac{C_{mag}}{ne} \frac{1}{1+\tau_{em}/\tau_m}.$$

Here, τ_{em} is the electron-magnon scattering time and τ_m is the total magnon scattering time for all magnon scattering events (i.e., electron-magnon, phonon-magnon, magnon-magnon) respectively. Note that $\tau_{em} \geq \tau_m$ holds by definition. If $\tau_{em} \gg \tau_m$ holds (indicating weak electron-magnon coupling), the drag contribution in S_{xx} becomes negligible. On the other hand, if $\tau_{em} \sim \tau_m$ holds (indicating strong electron-magnon coupling), then the temperature dependence of drag contribution in $S_{xx}(T)$ is governed by $C_{mag}(T)$. Importantly, based on magnon picture, $C_{mag}(T)$ shows logarithmic temperature dependence T^n , and C_{mag} of FM and AFM magnons are known to exhibit $n \sim 1.5$ and $n \sim 3$, respectively⁴⁷. In our case, $|\Delta S_B|$ is expected to reflect $|\Delta S_{xx}|$, and it is a reasonable simplification not to consider a phonon drag contribution since our $|\Delta S_B|$ is dominated nearby magnetic phase transition temperature T_C .

Existence of exponent $n \sim 3$

To check for the existence of a logarithmic temperature dependence of $|\Delta S_B(T)|$ near T_C , we first show $\log(\Delta S_B)$ vs. $\log(T)$ plot in **Fig. 3b-d**. From this plot, the existence of a logarithmic temperature dependence of $|\Delta S_B(T)|$ near T_C is visually discernable from the linear dependence. Indeed, around T_C , a clear linearity can be recognized from $\log(\Delta S_B)$ vs. $\log(T)$ plots of the three doping levels $\delta = 0.5, 0.54, \text{ and } 0.68$. From the fitting of the temperature region between T_C and ~ 100 K below T_C at each doping level, the exponents n for three doping levels $\delta = 0.5, 0.54, \text{ and } 0.68$ are 3.2, 2.8, and 2.7, respectively (see lined in **Fig. 3b-d**). We also show the temperature dependence of the slope as defined by following equation $n(T) = \partial\{\log(\Delta S_B) - \log(T)\}/\partial \log(T)$. From the plot shown in **Fig. 3e**, this slope n is almost constant near T_C , and the averaged estimated value of n at each of the three doping levels in this temperature region is around $n \sim 3$. Phenomenologically, our observation of an $n = 3$ at three different doping levels of $\delta \geq \delta_C$ strongly implies the existence of AF magnon

drag with $\tau_{em} \sim \tau_m$, rather than an $n \sim 1.5$ based FM magnon picture. While the drag effect is seen mainly at very low temperatures where electron-boson coupling is strong, our magnon case shows a dominant drag contribution around T_C . The potential reason leading to $\tau_{em} \sim \tau_m$ is our nature of magnetism in our system, which at the cusp of itinerant and localized magnetism. Although quantifying τ_{em} and τ_m are generally challenging, similar magnon contributions have been observed near T_C in several magnetic materials^{48,49,50}.

Nature of critical doping

Our most intriguing finding beyond the existing literature on the Cr-Te system^{27,51,52,53,54} is the existence of a critical doping (δ_c). From a previous DFT study, FM interactions couple Cr atoms along the in-plane direction on one sublattice, while AFM interactions couple Cr atoms along the out-of-plane direction on the other sublattice, in the case of CrTe ($\delta = 1$) with two clearly differentiated magnetic Cr sublattices³⁸. Even in the critical case of $\delta_c \sim 0.5$, it is natural to assume the coexistence of FM and AFM interactions, as shown in **Fig. 4c**. Intriguingly, the experimental realization of $K_{eff} \sim 0$ around δ_c is expected to reflect a particularly unique situation where the competition between multiple magnetic interactions and a correspondingly large frustration leads to enhanced magnetic fluctuations³⁸. Notably, the dominant exponent $n \sim 3$ around critical doping (**Fig. 3**) is consistent with expected crucial role of AFM based fluctuations.

Electronic structure perspectives

We speculate that the magnetic fluctuation driven enhancement of S_{xx} around δ_c is also linked to the anomaly in the electronic state around this critical doping level. This notion is supported by the fact that $E_0 - E_F = 0$ is realized around $\delta_c \sim 0.5$. As indicated previously, while a metallic hole band occurs near the $\bar{\Gamma}$ point at all doping levels, a pseudogap in the density of states at E_F occurs exclusively at δ_c (see **Fig. 1c** and **d**). Therefore, we suspect that enhanced magnetic fluctuations alongside the pseudogap formation at E_F in the δ_c sample cooperatively drive the observed enhancement in the zero-field thermoelectric energy conversion around T_C . There are two paradigms by which to interpret such a cooperation. The first relies solely on the experimentally observed band structure around the \bar{M} point from ARPES, disregarding the energy dependence of the scattering rate $\alpha(E)$. This picture is justified by the factor $1/N(E)$ in an application of Equation (2) to our observations, since the position $E_0 - E_F = 0$ is expected to lead a dip in $N(E)$ (i.e., a pseudogap). A second and more holistic paradigm would be to consider the asymmetry in $\alpha(E)$ relative to E_F , in addition to expected pseudogap in $N(E)$. For instance, such asymmetric $\alpha(E)$ can be realized if a characteristic energy for an electronic state sensitive to the spin orientation and its fluctuations exists away from E_F . Although modeling of the microscopic underpinnings of these observations in S_{xx} is anticipated as a future undertaking, it can be expected that a significant spin-orbit coupling effect arising from the presence of the heavy element Te plays a role in bridging between the spin and charge degrees of freedom near E_F in $\text{Cr}_{1+\delta}\text{Te}_2$.

Summary

A systematic investigation of the doping, temperature, and magnetic field dependence of the longitudinal thermoelectric response S_{xx} is presented in the electronically/magnetically tunable semimetal $\text{Cr}_{1+\delta}\text{Te}_2$. We show

signatures of magnetic fluctuation-driven enhancement of longitudinal thermoelectric response S_{xx} around a critical doping level $\delta \sim 0.5$, where antiferromagnetic fluctuations and near-Fermi-energy pseudogap play a potential vital role in enhancing thermoelectric energy conversion.

We emphasize that detection of a magnetically modulated thermoelectric signal necessitates coupling between the magnetic and charge degrees of freedom. While a solid understanding of the underlying electronic states is always crucial in interpreting such charge-spin coupling, direct spectroscopic evidence of the electronic structure has been lacking from most studies in magnetic/metallic thermoelectric materials so far. As such, this study, which bridges between momentum space electronic states and thermoelectric effects in the tunable magnetic semimetal $\text{Cr}_{1+\delta}\text{Te}_2$, provides valuable clarifying information regarding the interplay between magnetism and thermoelectricity. Finally, the fact that $\text{Cr}_{1+\delta}\text{Te}_2$ has been identified as an intriguing material platform that hosts Berry curvature physics in real and momentum spaces also suggests the possibility of exotic intertwined effects between the anomalous thermoelectric response and Berry curvature physics to be pursued in future investigations of this material, including study of transverse thermoelectric effect.

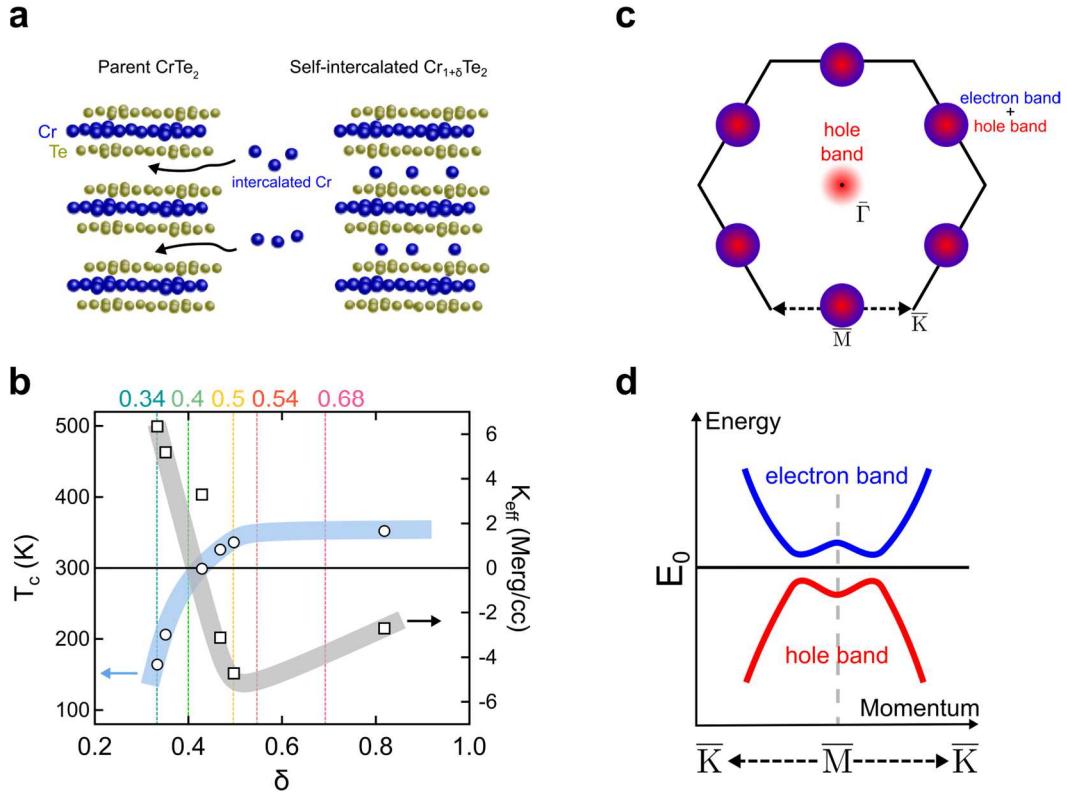


Fig. 1 Magnetic and electronic tunability of $\text{Cr}_{1+\delta}\text{Te}_2$. **a** Schematic for self-intercalation of Cr atoms in the parent CrTe_2 . **b** Doping evolution of the Curie temperature (T_c) and magnetic anisotropy energy (K_{eff}) as previously determined from [38]. The colored lines indicate the compositions investigated in this study. **c** Schematic of the k -space electronic structure determined from ARPES studies on $\text{Cr}_{1+\delta}\text{Te}_2$ [39]. Around $\bar{\Gamma}$, the hole band dominates near the Fermi energy. However, the coexistence of electron and hole bands around \bar{M} points constitute a semimetallic band portion. **d** The schematic semimetallic band portion around \bar{M} from **c**. The characteristic energy (E_0) is the charge neutral point of the semimetallic band portion corresponding to a pseudogap.

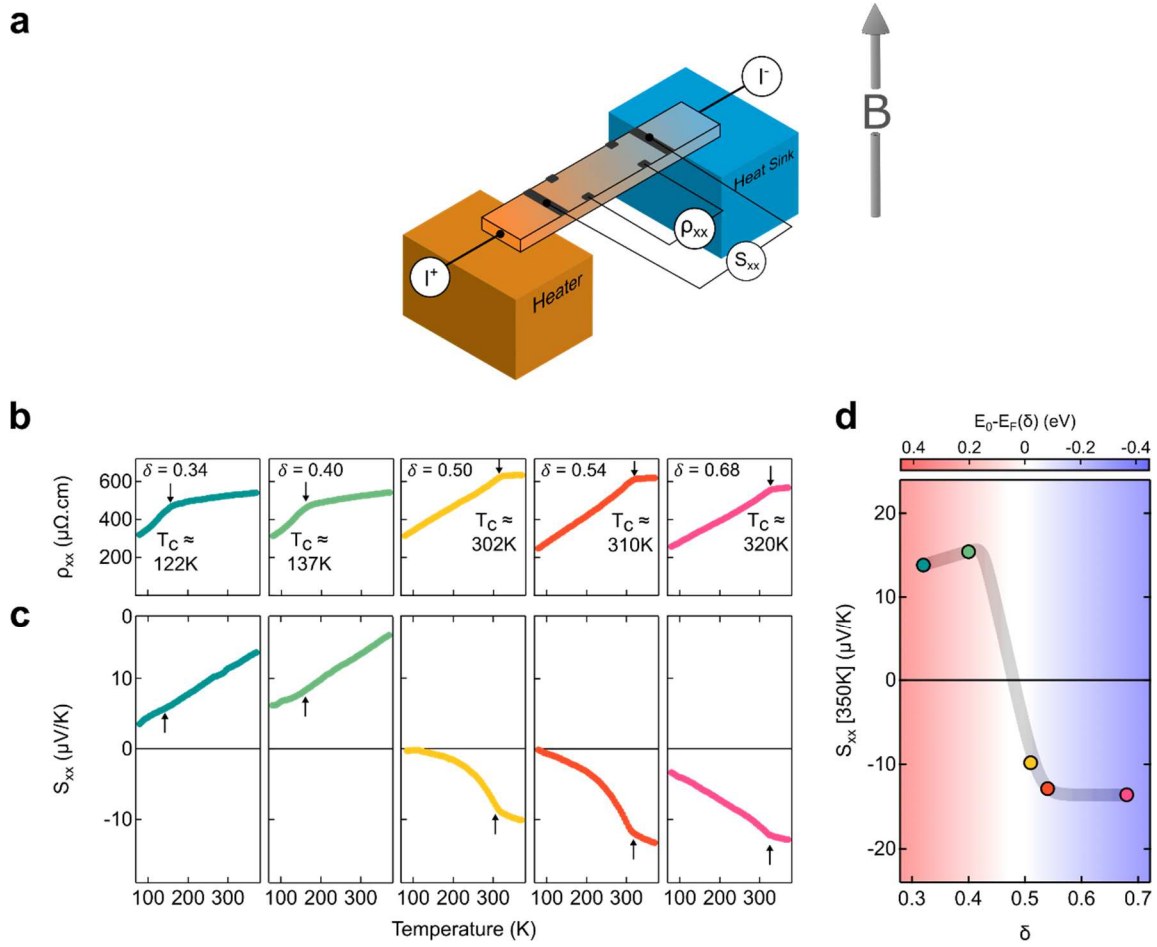


Fig. 2 Evolution of the transport properties in (001) oriented epitaxial $\text{Cr}_{1+\delta}\text{Te}_2$ films grown on Al_2O_3 (0001) substrates. **a** Electrode configuration for simultaneous measurement of longitudinal resistivity (ρ_{xx}) and thermopower (S_{xx}). The B -field is applied parallel to $\text{Cr}_{1+\delta}\text{Te}_2(001)$ direction. **b** Temperature and doping evolution of ρ_{xx} . T_C is estimated from the kinks in $\rho_{xx}(T)$. **c** Temperature dependence of S_{xx} . Arrows denote T_C from **b**. **d** Doping evolution of S_{xx} at 350 K with $E_0 - E_F(\delta)$ from [39] overlaid as a gradient showing a clear sign crossover in both quantities around $\delta = 0.5$.

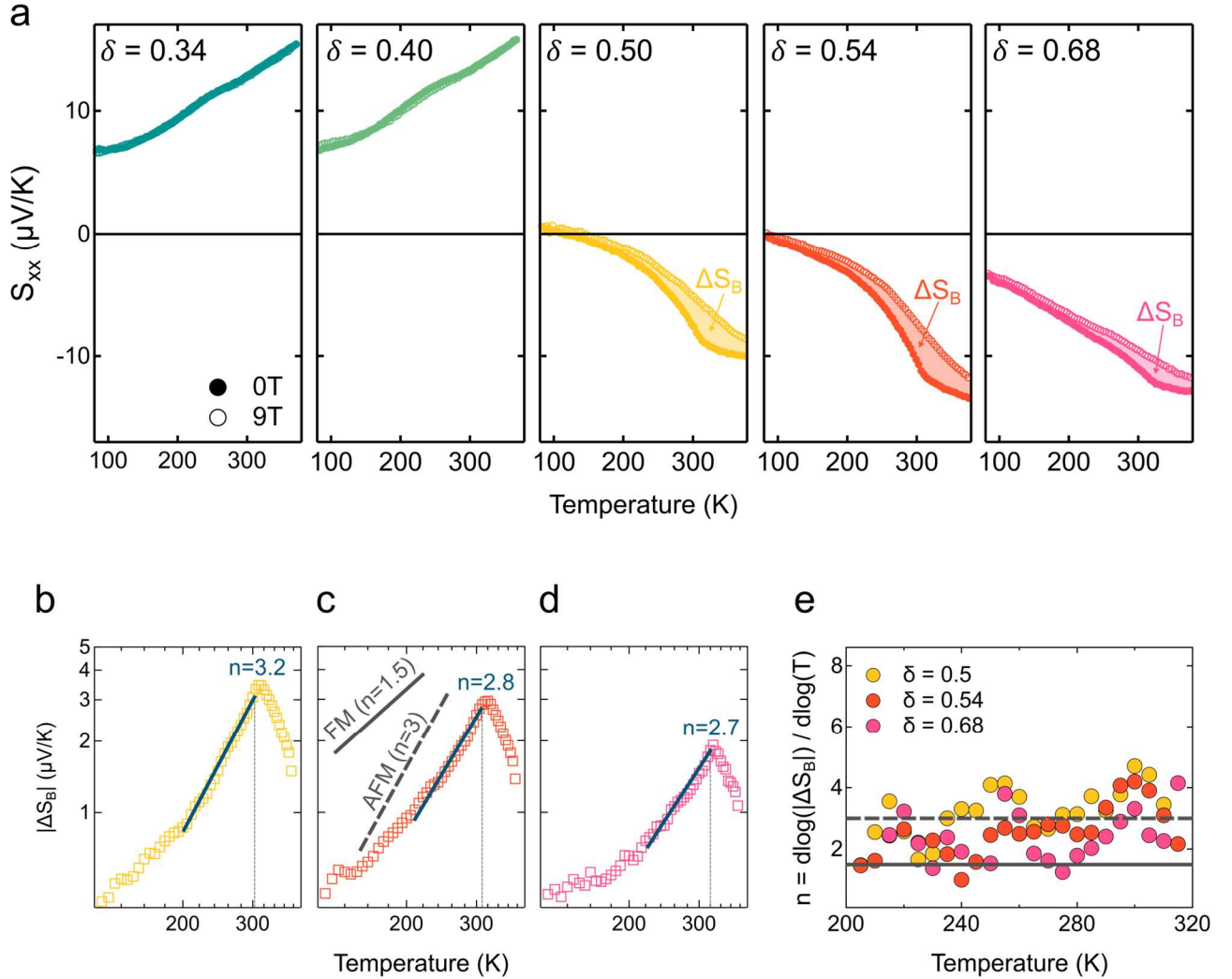


Fig. 3 Doping evolution of the magneto thermopower. **a** Comparison between the thermopowers at 0 and 9 T for the five doping levels. A significant difference between $S_{xx}(0\text{ T})$ and $S_{xx}(9\text{ T})$ can be seen in the $\delta = 0.5$ and $\delta = 0.54$, indicated by the shaded regions and defined as ΔS_B . **b-d** log-log plots of $|\Delta S_B| = |S_{0\text{ T}} - S_{9\text{ T}}|$ for the $\delta = 0.5$, 0.54 and 0.68 samples. T_C is indicated at each doping level by the thin grey line. Power fits of the linear regions (between T_C and ~ 100 K below T_C) on the log-log plot are indicated by the solid blue lines with T^n exponents indicated. The slopes on the log-log plots corresponding to FM and AFM magnons are indicated by the solid and dashed grey lines in **c**. **e** The temperature dependence of the fitting exponent n determined by $n(T) = \partial \{ \log(\Delta S_B) - \log(T) \} / \partial \log(T)$ for the three doping levels ($\delta = 0.5$, $\delta = 0.54$ and $\delta = 0.68$). The solid and broken lines in **c** and **e** are n for FM and AFM cases.

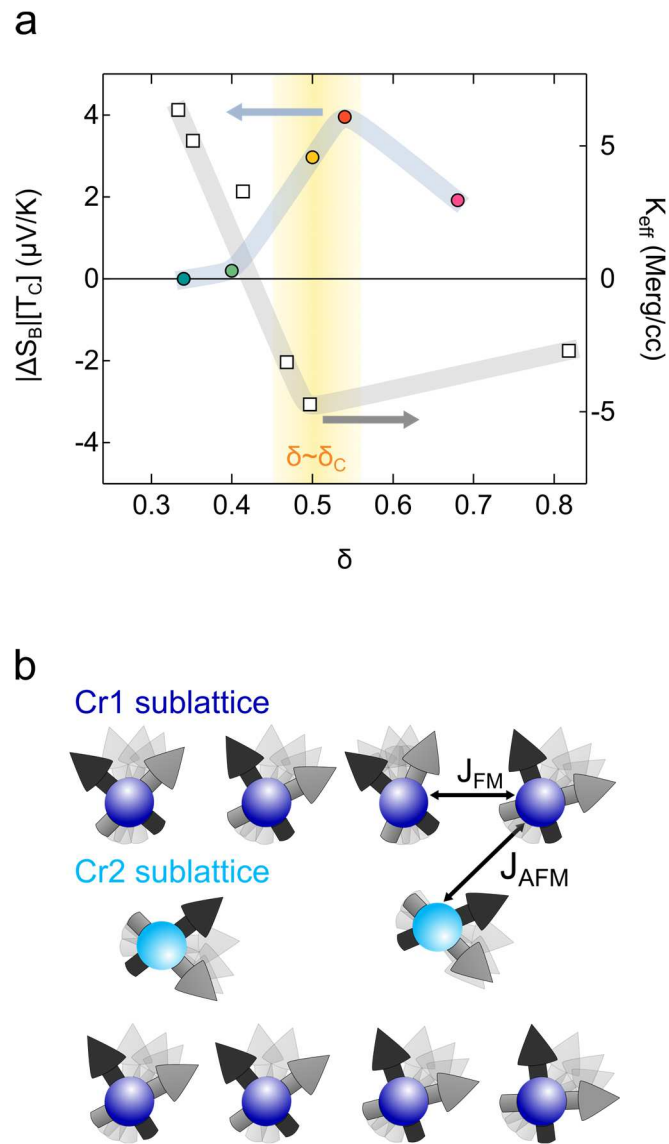


Fig. 4 Existence of critical doping with AFM-enhanced magnetic fluctuations. **a** The phenomenological correspondence between the doping evolution of $|\Delta S_B(T_C)|$ (left axis) and that of K_{eff} (right axis). Shaded regions are meant simply as a guide to the eye for critical region (see main body for details). **b** The schematic for magnetic competition and enhanced fluctuation around critical doping.

References

- ¹ L. E. Bell, *Science* **321**, 1457 (2008).
- ² W. Koshibae, K. Tsutsui, and S. Maekawa, *Phys Rev B* **62**, 6869 (2000).
- ³ I. Terasaki, Y. Sasago, and K. Uchinokura, *Phys Rev B* **56**, R12685 (1997).
- ⁴ Y. Wang, N. S. Rogado, R. J. Cava, and N. P. Ong, *Nature* **423**, 425 (2003).
- ⁵ T. Takeuchi, T. Kondo, T. Takami, H. Takahashi, H. Ikuta, U. Mizutani, K. Soda, R. Funahashi, M. Shikano, M. Mikami, S. Tsuda, T. Yokoya, S. Shin, and T. Muro, *Phys Rev B* **69**, 125410 (2003).
- ⁶ G. E. W. Bauer, E. Saitoh, and B. J. van Wees, *Nat Mater* **11**, 391 (2012).
- ⁷ K. Uchida, S. Takahashi, K. Harii, J. Ieda, W. Koshibae, K. Ando, S. Maekawa, and E. Saitoh, *Nature* **455**, 778 (2008).
- ⁸ K. Uchida, J. Xiao, H. Adachi, J. Ohe, S. Takahashi, J. Ieda, T. Ota, Y. Kajiwara, H. Umezawa, H. Kawai, G. E. W. Bauer, S. Maekawa, and E. Saitoh, *Nat Mater* **9**, 894 (2010).
- ⁹ M. V. Costache, G. Bridoux, I. Neumann, and S. O. Valenzuela, *Nat Mater* **11**, 199 (2012)
- ¹⁰ Md. M. H. Polash, F. Mohaddes, M. Rasoulianboroujeni, and D. Vashae, *J Mater Chem C* **8**, 4049 (2020).
- ¹² N. Tsujii, A. Nishide, J. Hayakawa, and T. Mori, *Sci Adv* **5**, eaat5935 (2019).
- ¹³ T. Jungwirth, X. Marti, P. Wadley, and J. Wunderlich, *Nat Nanotechnol* **11**, 231 (2016).
- ¹⁴ S. K. Kim, G. S. D. Beach, K.-J. Lee, T. Ono, T. Rasing, and H. Yang, *Nat Mater* **21**, 24 (2022).
- ¹⁵ S. Nakatsuji and R. Arita, *Annu Rev Condens Ma P* **13**, (2021).
- ¹⁶ C. Fu, Y. Sun, and C. Felser, *Appl. Mater*, **8**, 040913, (2020).
- ¹⁷ Y. Fujishiro, N. Kanazawa, T. Shimojima, A. Nakamura, K. Ishizaka, T. Koretsune, R. Arita, A. Miyake, H. Mitamura, K. Akiba, M. Tokunaga, J. Shiogai, S. Kimura, S. Awaji, A. Tsukazaki, A. Kikkawa, Y. Taguchi, and Y. Tokura, *Nat Commun* **9**, 408 (2018).
- ¹⁸ C. Han, Q. Sun, Z. Li, and S. X. Dou, *Adv Energy Mater*, **6**, 1600498 (2016).
- ¹⁹ J. Yan, X. Luo, X. Luo, G. Lin, F. Chen, J. Gao, Y. Sun, Y. Sun, Y. Sun, Y. Sun, L. Hu, P. Tong, W. Song, Z. Sheng, W. Lu, X. Zhu, and Y. Sun, *Epl-Europhys Lett* **124**, 67005 (2019).

-
- ²⁰ Y. Wang, J. Yan, J. Li, J. Li, S. Wang, S. Wang, S. Wang, S. Wang, S. Wang, M. Song, J. Song, Z. Li, K. Chen, K. Chen, Y. Qin, L. Ling, H. Du, L. Cao, X. Luo, X. Luo, Y. Xiong, and Y. Sun, *Phys Rev B* **100**, 024434 (2019).
- ²¹ Z. Jiang, Z. Z. Jiang, X.-D. Luo, X. Luo, J.-M. Yan, J. Gao, J.-H. Gao, W. H. Wang, W. H. Wang, W. H. Wang, G. Zhao, G. C. Zhao, Y. Sun, Y. Sun, J. G. Si, W. Lu, W. J. Lu, P. Tong, X. Zhu, W. H. Song, and Y. P. Sun, *Phys Rev B* **102**, 144433 (2020).
- ²² H. Takasu, T. Hashimoto, H. Kazuo, K. Hoya, M. Yamaguchi, Y. Masuhiro, I. Ichitsubo, and I. Ikuro, *J Phys Soc Jpn* **31**, 679 (1971).
- ²³ J. Dijkstra, H. H. Weitering, H. H. Weitering, C. F. van Bruggen, C. F. van Bruggen, C. Haas, C. Haas, and R. A. de Groot, *J Phys Condens Matter* **1**, 9141 (1989).
- ²⁴ M. Yamaguchi and T. Hashimoto, *J Phys Soc Jpn* **32**, 635 (1972).
- ²⁵ K. Oda, S. Yoshii, Y. Yasui, M. Ito, T. Ido, Y. Ohno, Y. Kobayashi, and M. Sato, *J Phys Soc Jpn* **70**, 2999 (2001).
- ²⁶ L.-Z. Zhang, A.-L. Zhang, X.-D. He, X.-W. Ben, Q.-L. Xiao, W. Lu, F. Chen, F. Chen, Z. Feng, S. Cao, J. Zhang, and J.-Y. Ge, *Phys Rev B* **101**, 214413 (2020).
- ²⁷ G. Cao, G. Cao, Q. Zhang, Q. Zhang, M. Frontzek, W. Xie, D. Gong, D. Gong, G. E. Sterbinsky, and R. Jin, *Phys Rev Mater* **3**, 125001 (2019).
- ²⁸ O. Akira, A. Ohsawa, Y. Yamaguchi, Y. Yasuo, N. Kazama, K. Noriaki, Y. Hiroshi, H. Yamauchi, H. Yamauchi, W. Hiroshi, H. Watanabe, and H. Watanabe, *J Phys Soc Jpn* **33**, 1303 (1972).
- ²⁹ X. Zhang, X. Zhang, Q. Lu, W. Liu, W. Niu, N. Wei, J. Sun, J. Cook, J. Cook, J. Cook, J. Cook, M. Vaninger, P. F. Miceli, D. J. Singh, S.-W. Lian, T.-R. Chang, X. He, X. He, J. Du, L. He, R. Zhang, G. Bian, and Y. Xu, *Nat Commun* **12**, 2492 (2021).
- ³⁰ M. Huang, L. Gao, Y. Zhang, Y. Zhang, X. Lei, X. Lei, G. Hu, J. Xiang, H. Zeng, H. Zeng, H. Zeng, X. Fu, X. Fu, Z. Zhang, G. Chai, G. Chai, Y. Peng, Y. Lu, H. Du, G. Chen, G. Chen, J. Zang, and B. Xiang, *Nano Lett* **21**, 4280 (2021).
- ³¹ Y. He, J. Kroder, J. Gayles, C. Fu, Y. Pan, W. Schnelle, C. Felser, and G. H. Fecher, *Appl Phys Lett* **117**, 052409 (2020).
- ³² L.-Z. Zhang, X.-D. He, A.-L. Zhang, A.-L. Zhang, Q.-L. Xiao, W. Lu, F. Chen, F. Chen, F. Chen, F. Chen, Z. Feng, S. Cao, S. Cao, J. Zhang, and J.-Y. Ge, *Apl Mater* **8**, 031101 (2020).
- ³³ J.-J. Xian, C. Wang, J.-H. Nie, R. Li, M. Han, J. Lin, W.-H. Zhang, Z. Liu, Z. Zhang, M.-P. Miao, Y. Yi, S. Wu, X. Chen, J. Han, Z. Xia, W. Ji, and Y.-S. Fu, *Nat Commun* **13**, 257 (2022).

-
- ³⁴ Y. Gong, J. Sun, W. Hu, S. Li, W. Xu, G. Tan, and X. Tang, *Appl. Phys. Lett.* **120**, 023905 (2022)
- ³⁵ M. Huang, S. Wang, Z. Wang, P. Liu, J. Xiang, C. Feng, X. Wang, Z. Zhang, Z. Wen, H. Xu, G. Yu, Y. Lu, W. Zhao, S. A. Yang, D. Hou, and B. Xiang, *ACS Nano* **15**, 9759 (2021)
- ³⁶ Z. Jin, Z. Ji, Y. Zhong, Y. Jin, X. Hu, X. Zhang, L. Zhu, X. Huang, T. Li, X. Cai, and L. Zhou, *ACS Nano* **16**, 7572 (2022)
- ³⁷ R. Chua, J. Zhou, X. Yu, W. Yu, J. Gou, R. Zhu, L. Zhang, M. Liu, M. B. H. Breese, W. Chen, K. P. Loh, Y. P. Feng, M. Yang, Y. L. Huang, and A. T. S. Wee, *Adv. Mater.* **33**, 2103360 (2021)
- ³⁸ Y. Fujisawa, M. Pardo-Almanza, J. Garland, K. Yamagami, K. Yamagami, K. Yamagami, X. Zhu, X. Chen, K. Araki, T. Takeda, M. Kobayashi, Y. Takeda, C. H. Hsu, C.-H. Hsu, F.-C. Chuang, F.-C. Chuang, R. Laskowski, R. Laskowski, K. H. Khoo, A. Soumyanarayanan, A. Soumyanarayanan, and Y. Okada, *Phys Rev Mater* **4**, 114001 (2020).
- ³⁹ Y. Fujisawa, M. Pardo-Almanza, C. H. Hsu, A. Mohamed, K. Yamagami, A. Krishnadas, F. C. Chuang, K. H. Khoo, J. Zang, A. Soumyanarayanan, and Y. Okada, *Arxiv* (2022).
- ⁴⁰ N. P. Ong, *Phys Rev B* **43**, 193 (1991).
- ⁴¹ S. Hébert, R. Daou, A. Maignan, S. Das, A. Banerjee, Y. Klein, C. Bourgès, N. Tsujii, and T. Mori, *Sci Technol Adv Mat* **22**, 583 (2021).
- ⁴² B. D. Cullity and C. D. Graham, *Introduction to Magnetic Materials* (John Wiley & Sons, 2011).
- ⁴³ T. Moriya, *Spin Fluctuations in Itinerant Electron Magnetism* (Springer Science & Business Media, 1985).
- ⁴⁴ S. J. Watzman, R. A. Duine, Y. Tserkovnyak, S. R. Boona, H. Jin, A. Prakash, Y. Zheng, and J. P. Heremans, *Phys Rev B* **94**, 144407 (2016).
- ⁴⁵ Y. Zheng, T. Lu, M. M. H. Polash, M. Rasoulianboroujeni, N. Liu, M. E. Manley, Y. Deng, P. J. Sun, X. L. Chen, R. P. Hermann, D. Vashaee, J. P. Heremans, and H. Zhao, *Sci Adv* **5**, eaat9461 (2019).
- ⁴⁶ T. Okabe, *J Phys Condens Matter* **22**, 115604 (2010).
- ⁴⁷ J.P. Heremans, *Thermal spin transport and spin in thermoelectrics*, In “Advances in Thermoelectricity: Foundational Issues, Materials and Nanotechnology” (IOP Publishing, 2021)
- ⁴⁸ J. D. Wasscher and C. Haas, *Phys Lett* **8**, 302 (1964).
- ⁴⁹ M. Yokonuma, M. Wakatsuki, Y. Kusada, T. Koyanagi, and K. Matsubara, *J Magnetism Soc Jpn* **19**, 723 (1995).

-
- ⁵⁰ Y. Zheng, T. Lu, M. M. H. Polash, M. Rasoulianboroujeni, N. Liu, M. E. Manley, Y. Deng, P. J. Sun, X. L. Chen, R. P. Hermann, D. Vashaee, J. P. Heremans, and H. Zhao, *Sci Adv* **5**, eaat9461 (2019).
- ⁵¹ Z. Jiang, Z. Z. Jiang, X.-D. Luo, X. Luo, J.-M. Yan, J. Gao, J.-H. Gao, W. H. Wang, W. H. Wang, W. H. Wang, G. Zhao, G. C. Zhao, Y. Sun, Y. Sun, J. G. Si, W. Lu, W. J. Lu, P. Tong, X. Zhu, W. H. Song, and Y. P. Sun, *Phys Rev B* **102**, 144433 (2020).
- ⁵² R. Mondal, R. Kulkarni, A. Thamizhavel, and A. Thamizhavel, *J Magn Magn Mater* **483**, 27 (2019).
- ⁵³ M. H. Polash and D. Vashaee, *Iscience* **24**, 103356 (2021).
- ⁵⁴ Q. H. Li, S. Li, S. Li, D. Wu, Z.-K. Ding, X.-H. Cao, L. Huang, H. Pan, B. Li, B. Li, K.-Q. Chen, and X. Duan, *Appl Phys Lett* **119**, 162402 (2021).